



MOFs-derived ultrathin holey Co_3O_4 nanosheets for enhanced visible light CO_2 reduction

Weiyi Chen^{a,b}, Bin Han^{a,b}, Chen Tian^{a,b}, Xueming Liu^{a,b}, Shujie Liang^{a,b}, Hong Deng^{a,b,*}, Zhang Lin^{a,b,*}

^a School of Environment and Energy, Key Laboratory of Pollution Control and Ecosystem Restoration in Industry Clusters (Ministry of Education), South China University of Technology, Guangzhou 510006, China

^b Guangdong Engineering and Technology Research Center for Environmental Nanomaterials, South China University of Technology, Guangzhou 510006, China



ARTICLE INFO

Keywords:
 CO₂ Reduction
 Photocatalysis
 MOFs derived
 Ultrathin nanosheets
 Co_3O_4

ABSTRACT

Reducing carbon dioxide (CO₂) to various value-added chemical products by photocatalysis could effectively alleviate the serious problems of global warming and energy shortages. Currently, most commonly prepared photocatalysts present poor performance under visible light irradiation. In this study, we adopted a facile, scalable and controllable approach to prepare ultrathin two-dimensional (2D) porous Co_3O_4 catalysts (Co_3O_4 -NS) by air calcining of the ultrathin metal-organic framework (MOFs) nanosheet templates to validly reduce CO₂ with a Ru-based photosensitizer under visible light irradiation. Benefiting from the structural nature of MOFs precursors, the calcined Co_3O_4 -NS inherit the morphology of 2D and well-developed porosity, which support the transport of electrons, enhance the adsorption of CO₂ molecules, and render abundant catalytic sites for CO₂ activation. As a result, the CO generation rate is approximately 4.52 $\mu\text{mol}\cdot\text{h}^{-1}$ with selectivity of 70.1%, which is superior to the Co_3O_4 bulk catalysts (Co_3O_4 -BK). Additionally, density functional theory (DFT) calculations reveal that the model of Co_3O_4 monolayer has stronger CO₂ adsorption energy than that of the Co_3O_4 bulk, which is beneficial for the CO₂-to-CO conversion. This MOF-engaged strategy provides new insight into the controlled synthesis of advanced ultrathin holey nanosheets to improve the efficiency of photocatalytic CO₂ reduction.

1. Introduction

Reduction of CO₂ to various value-added chemical products using clean, recyclable solar energy can simultaneously address the serious problems of global warming and energy shortages [1–5]. However, photocatalytic CO₂ reduction generally suffers from low energy conversion efficiency due to the high thermodynamic stability of the linear CO₂ molecule [6]. Notably, the development and modification of catalysts is one of the most functional methods to improve the CO₂ photoreduction efficiency. Transition metal ions/complexes with multiple redox states have been widely investigated as favourable catalysts to facilitate the photocatalytic conversion of CO₂ in combination with appropriate light harvesters [7–12]. In particular, cobalt oxides/complexes have been demonstrated to accelerate charge transport and strengthen CO₂ adsorption/activation in CO₂ photoreduction systems [7,13–17]. Unfortunately, it is difficult to achieve remarkable perfor-

mance using conventional transition metal catalysts, mainly due to a high recombination rate of the photoinduced electron-hole pairs, as well as a low ratio of the catalytically active sites, which arise from their limitations with respect to morphology and size [6,18–20]. Therefore, to achieve better photochemical CO₂ conversion performance, the precise fabrication of catalysts with suitable structure is still urgently needed.

Among the numerous available nanostructures, ultrathin 2D nanosheets have attracted considerable attention in environmental and energy related catalytic areas in recent years [21]. With regard to the CO₂ photoreduction, the high specific surface area of the ultrathin 2D materials is beneficial for the substance transport that can increase the contact between the catalyst surface and CO₂. Additionally, the atomic-level thickness could effectively shorten the diffusion length of the electrons, enhancing the utilization of the photoinduced electrons in the catalysts. More importantly, ultrathin 2D materials are more likely to

* Corresponding authors at: School of Environment and Energy, Key Laboratory of Pollution Control and Ecosystem Restoration in Industry Clusters (Ministry of Education), South China University of Technology, Guangzhou 510006, China.

E-mail addresses: dengh2016@scut.edu.cn (H. Deng), zlin@scut.edu.cn (Z. Lin).

expose a high number of catalytically active sites for the CO₂ photoreduction [22,23]. These features of ultrathin 2D materials are highly desirable for promoting photocatalytic CO₂ reactions relative to their corresponding bulk counterparts. Indeed, several significant studies have confirmed the remarkable promise of CO₂ photoreduction by ultrathin 2D materials [24–27]. Furthermore, nanosheets with numerous in-plane holes are highly desirable because the holes are more accessible and could promote the electron and mass transport across the planes during the photocatalytic process. Conversely, these holes will not only expose many more catalytic sites but also prevent their aggregation by significantly reducing the interaction sites [28]. However, relative to the above remarkable potential, the effective control of well-defined structures presents major obstacles to further advances. Thus, it is urgently necessary to explore effective strategies for fabricating ultrathin 2D holey materials.

Currently, MOFs, as a new class of crystalline and porous materials that consist of metal ions and organic ligands, have been recognized as functional materials that serve as sacrificial templates for construction of various nanomaterials [29,30]. First, based on the reasonable selection of reactants and reaction conditions, MOFs derivatives with the desired composition and shape can be easily obtained [31]. Second, nanomaterials derived from MOFs can maintain the characteristics of the large specific surface area and well-developed porosity, which are advantageous for photocatalysis [32–34]. Under appropriate treatments, MOFs can be converted to carbon, metal oxides, metal sulphides, metal phosphates or other metal compounds while retaining the original structure [35]. Based on the above advantages, it is possible to directly synthesize ultrathin 2D holey materials using ultrathin 2D MOFs as precursors to overcome the low yield and uncontrollable defects that are obtained using traditional methods of 2D materials synthesis, such as mechanical exfoliation, and liquid exfoliation [36]. For instance, Zhang, et al. obtained the CoS_{1.097}/nitrogen-doped carbon composite through the sulphidation of the PPF-3 MOF nanosheets that has been regarded as one of the extraordinary landmarks in the progress of construction and application of MOF-derived nanomaterials [37]. However, due to the limitations of the synthetic methods used to obtain 2D MOFs, there have been only a few reports on direct preparation and property studies of ultrathin holey nanosheets derived from MOFs precursors.

Given the superiority of MOFs templates in the construction of nanomaterials and the apparent merits of ultrathin 2D porous structures for CO₂ photoreduction, we effectively synthesized ultrathin holey Co₃O₄ nanosheets with a thickness of ~1.8 nm by air calcining of ultrathin MOFs nanosheets. Subsequently, the prepared Co₃O₄-NS were applied as catalysts with Ru-based photosensitizers for photocatalytic CO₂ reduction. Compared to bulk Co₃O₄, Co₃O₄-NS have enhanced activity and selectivity for CO₂-to-CO conversion that may stem from the synergistic effect of the stronger CO₂ adsorption performance, faster charge migration ability, and greater number of exposed active sites. These results offer a novel avenue for the design and synthesis of catalysts for highly efficient photocatalytic CO₂ reduction.

2. Experimental

2.1. Chemicals

All of the chemicals used in this work were used as received without further purification, including cobalt nitrate hexahydrate (Co(NO₃)₂·6H₂O, 99%, Aladdin), 2-Methylimidazole (2-MIM, 98%, Aladdin), [Ru(bpy)₃]Cl₂·6H₂O (bpy = 2,2-bipyridine, 98%, Innochem), triethanolamine (TEOA, > 99.0%, Aladdin), acetonitrile (MeCN, > 99.5%, Aladdin), anhydrous methanol (> 99.5%), ultra-purity carbon dioxide (99.9999%) and ultra-purity argon (99.9999%), the gas was supplied by Foshan Ms Messer Gas Co., Ltd.

2.2. Synthesis of materials

Synthesis of ZIF-67: the synthesis of ZIF-67 sample was performed according to the method reported in the literature with a slight modification [38]. First, Co(NO₃)₂·6H₂O (0.546 g) and 2-methylimidazole (0.616 g) were dissolved in methanol (15 mL) to form solutions A and B, respectively. Then, solution A was slowly added to solution B in 1 min followed by ultrasonication for 20 min. Finally, the purple ZIF-67 powders were obtained by washing in methanol several times followed by drying under vacuum at 65 °C overnight.

Synthesis of cobalt-based MOF nanosheet (Co-MOF-NS): the synthesis of Co-MOF-NS was similar to that reported in the literature with a slight modification [38]. The resultant ZIF-67 were dispersed in methanol (15 mL) and mixed with solution A. Then, the mixture was transferred into 50 mL Teflon-lined stainless-steel autoclaves and held at 120 °C for 1 h. The resultant yellow products were repeatedly washed in methanol and separated by centrifugation followed by vacuum drying at 65 °C for further use. We denoted the final product as Co-MOF-NS.

Synthesis of Co₃O₄-NS and Co₃O₄-BK: the Co-MOF-NS was placed in a crucible and calcined in a muffle furnace at 350 °C for 2 h with a ramping rate of 5 °C min⁻¹ to obtain Co₃O₄-NS. For comparison, ZIF-67 was treated using the same procedure to obtain Co₃O₄-BK. Additionally, an equal amount of Co-MOF-NS was calcined at 300, 400, and 450 °C, respectively, to harvest a series of Co₃O₄-NS calcined at different temperatures. For ease of discussion, unless otherwise indicated, all of the samples used for the characterizations were prepared with calcination at 350 °C.

2.3. Materials characterization

Field emission scanning electron microscopy (FE-SEM; Carl Zeiss MERLIN), and transmission electron microscopy (TEM, JEM-2100, JEOL Ltd.) images, high-resolution TEM images (HRTEM), and elemental mapping images were recorded to obtain information regarding the structure and element distribution. The thickness of the sample was characterized by atomic force microscopy (AFM, Asylum Research MFP-3D). Powder X-ray diffraction (XRD) was investigated using Bruker D8 AVANCE X-ray diffractometer with Cu K α to characterize the crystal structure of the samples. X-ray photoelectron spectroscopy (XPS) was performed with Thermo Fisher Scientific Escalab 250Xi X-ray photoelectron spectrometer using Al K α radiation to determine the surface composition of the samples. Fourier transform infrared spectroscopy (FT-IR) spectra of samples were collected on an RX1 PerkinElmer FT-IR spectrometer employing KBr as the diluter. The Brunauer-Emmett-Teller (BET) surface area and porous structure were detected by N₂ adsorption/desorption isotherms method with a Micromeritics ASAP 2020 analyser. Additionally, the CO₂ adsorption isotherms were analysed using a Micromeritics ASAP 2020 analyser at 298 K. All of the samples were degassed at 433 K for 8 h prior to the sorption measurements. The photoluminescence (PL) spectra were recorded using a Hitachi F-4600 instrument under 540 nm laser irradiation at room temperature. The measurements were carried out in an acetonitrile/water/triethanolamine (3 mL/2 mL/1 mL) solution containing [Ru(bpy)₃]Cl₂·6H₂O (7.5 mg), which is same as the photocatalytic CO₂ reduction process. Time-resolved transient PL decay spectra were carried out in the same solution as above. And the measurements were performed with EI FLS980 at room temperature. The UV-vis absorption spectra/ diffuse reflectance spectra (DRS) were obtained using a Shimadzu UV-2700 UV-vis spectrophotometer and BaSO₄ was used as the reflectance standard. Electrochemical measurements were performed using a CHI 660E electrochemical workstation in a typical three-electrode system: the prepared Co₃O₄-NS (Co₃O₄-BK)-modified ITO glass at the working electrode, the Pt net as

the counter electrode and an Ag/AgCl electrode as the reference electrode. Electrochemical impedance spectroscopy (EIS) measurements were conducted in the frequency range of 1 Hz to 100 KHz at the open-circuit voltage of 0 V, and the measurements were carried out in the solution containing acetonitrile/water/triethanolamine (3 mL/2 mL/1 mL). Mott – Schottky plots were collected in the range of -0.8 V to 0.8 V at a constant frequency of 10 KHz, and they were conducted in phosphate buffer saline (100 mM, pH = 7.4).

2.4. Photocatalytic CO₂ reduction

The photocatalysis experiments were performed by aggregating the catalysts and the photosensitizer [Ru(bpy)₃]Cl₂·6H₂O (7.5 mg) in an acetonitrile/water/ triethanolamine (3 mL/2 mL/1 mL) solution in a gas-closed quartz reactor (capacity of 75 mL). The entire reaction device was vacuum degassed, and the ultra-pure CO₂ (99.9999%) was introduced into the reaction device for 15 min to purge the air. A 5 W LED lamp (400 nm–1000 nm, Beijing Perfect Light Company, China) was used as the light source. The reaction system was vigorously stirred with a magnetic stirrer during the photocatalytic reactions. After illumination for a specific time, the generated products were detected by gas chromatography (Agilent 7890B). The apparent quantum efficiency (A.Q.E.) value for CO generation was determined at 420 nm using the same photochemical experimental device with a bandpass filter. The light intensity was measured by an optical power meter (Ceaulight), and the light intensity at 420 nm was 32.3 mW·cm⁻². The illuminated area was estimated to be 3.0 cm². For the recycling tests, the time of each cycle is 6 h. After 6 h irradiation, the same quality of new dye was added into the system and the ultra-pure CO₂ was introduced in the same method as described above to start the next cycle.

2.5. Computational details

First-principles density functional theory (DFT) calculations were performed using the Vienna Ab initio Simulation Package (VASP) package. The generalized gradient approximation (GGA) with the Perdew-Burke-Ernzerhof (PBE) functional was used to describe the electronic exchange and correlation effects. To describe the spinel structures of the Co₃O₄ atomic layer, a 2 × 2 unit cell of the most reactive Co³⁺ terminated (111) surface was used with ~15 Å of vacuum. Uniform G-centred k-point meshes with a resolution of 2π*0.03 Å⁻¹ and Methfessel-Paxton electronic smearing were adopted for the integration in the Brillouin zone for geometric optimization of the slab surfaces. The simulation was run with the cutoff energy of 550 eV throughout the calculations. These settings ensure the convergence of the total energies to within 1 meV per atom. Structure relaxation proceeded until forces on all of the atoms were less than 1 meV Å⁻¹ and the total stress tensor was within 0.01 GPa of the target value.

3. Results and discussion

Fig. 1 shows a schematic illustration of the synthesis process of Co₃O₄-NS. In brief, Co-ZIF-67 was first obtained by a rapid co-precipitation reaction of Co(NO₃)₂·6H₂O and 2-methylimidazole in the methanol solvent. Subsequently, a distinctive morphology conversion of the parent ZIF-67 from a rhombic dodecahedron to an ultrathin

cobalt-based MOF nanosheet was achieved by a solvothermal reaction in the presence of Co²⁺ (Figs. S1a-d, SI). With the structural evolution, the characteristic peaks of the XRD profiles changed from the parent ZIF-67 to the newly developed Co-MOF-NS, suggesting the occurrence of phase evolution (Fig. S2, SI), as is the case for the reported CoM-NS [39]. Finally, the Co-MOF-NS was converted to Co₃O₄-NS via calcination treatment in air. XRD profiles (Fig. S3, SI) show that the characteristic peaks of the Co₃O₄-NS at 18.9°, 31.3°, 36.8°, 38.5°, 44.8°, 55.7°, 59.4°, 65.2° and 78.4° correspond to the (111), (220), (311), (222), (400), (422), (511), (440) and (622) planes of cubic spinel Co₃O₄, respectively (JCPDS-74-2120). It is observed that enhanced calcination temperatures produce samples with higher crystallinities. In addition, the Co₃O₄-BK sample obtained by direct calcination of ZIF-67 at 350 °C shows similar XRD diffraction patterns. It's worth noting that the peaks intensity is weakened from Co₃O₄-BK to Co₃O₄-NS (350°C) since the nanosheets lack long-range atomic order in the third dimension [40]. To further verify the constituent elements and the valence states of the elements in the Co₃O₄-NS and Co₃O₄-BK sample, we performed XPS characterizations. As shown in Fig. S4a, the survey spectrum of both only display elemental peaks of C, Co, and O, and the inevitable presence of the C peak may be derived from adventitious carbon species. However, the positions of the core level orbitals of the cobalt element for Co₃O₄-NS show 0.3 eV shifts, to lower binding energy compared with that of Co₃O₄-BK. The binding energy shifts for the ultrathin nanosheets originate from the enhanced electron densities concentrated around the cobalt atoms, which owing to the dramatic distortion of the crystal structure [40,41]. Furthermore, for the high-resolution spectrum of Co 2p (Fig. S4b,c, SI), in addition to the apparent satellite peaks (denoted as "sat." in the figure), the binding energies at approximately 794.9, 779.9, 796.8 and 781.6 eV originated from the Co³⁺ 2p_{1/2}, Co³⁺ 2p_{3/2}, Co²⁺ 2p_{1/2} and Co²⁺ 2p_{3/2} spectra, respectively [42,43], confirming the successful fabrication of Co₃O₄. Moreover, except for the absorption bands of H₂O at 3473 and 1626 cm⁻¹ [43], the FT-IR spectrum of Co₃O₄-NS displays two distinct absorption bands at 662 and 565 cm⁻¹ that are attributed to the stretching vibrations of the Co-O bonds [44], indicating that pure Co₃O₄ was prepared without attachment of any organic capping agents (Fig. S5, SI).

SEM and TEM measurements were conducted to examine the structure and morphology of the Co₃O₄-NS. As displayed in **Fig. 2a** and b, the resultant Co₃O₄-NS products maintain the nanosheet morphology that is inherited perfectly from their MOF precursors. Additionally, large amounts of mesopores can be observed on the ultrathin nanosheets. Notably, the morphology of Co₃O₄-NS collapses when the temperature reaches 400 °C (Figs. S6a-c, SI). Additionally, the HRTEM image indicates a well-defined crystalline structure, in which the spacings between the lattice fringes with an angle of 60° are 0.285 nm, corresponding the planes perpendicular to the {111} facets of cubic spinel Co₃O₄ (PDF#74-2120) (**Fig. 2c**) [13]. Afterwards, the elementary mapping images clearly elucidate the uniform distribution of the Co and O elements (**Fig. 2d**). To gain further insights regarding the thickness of the Co₃O₄-NS sample, three positions were selected in a 10 × 10 μm area from the AFM image (**Fig. 2e**). As shown in **Fig. 2f**, the heights at positions 1, 2, and 3 in **Fig. 2e** correspond to 1.65 nm, 1.76 nm, and 2.03 nm, respectively, further confirming the ultrathin 2D structure. For the Co₃O₄-BK sample, an obvious bulk structure originated from ZIF-67 was observed (Fig. S6d, SI). BET analysis indicates

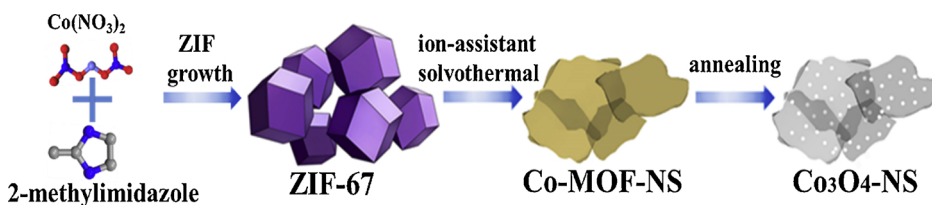


Fig. 1. Schematic illustration of the synthetic process of ultrathin holey Co₃O₄ nanosheets.

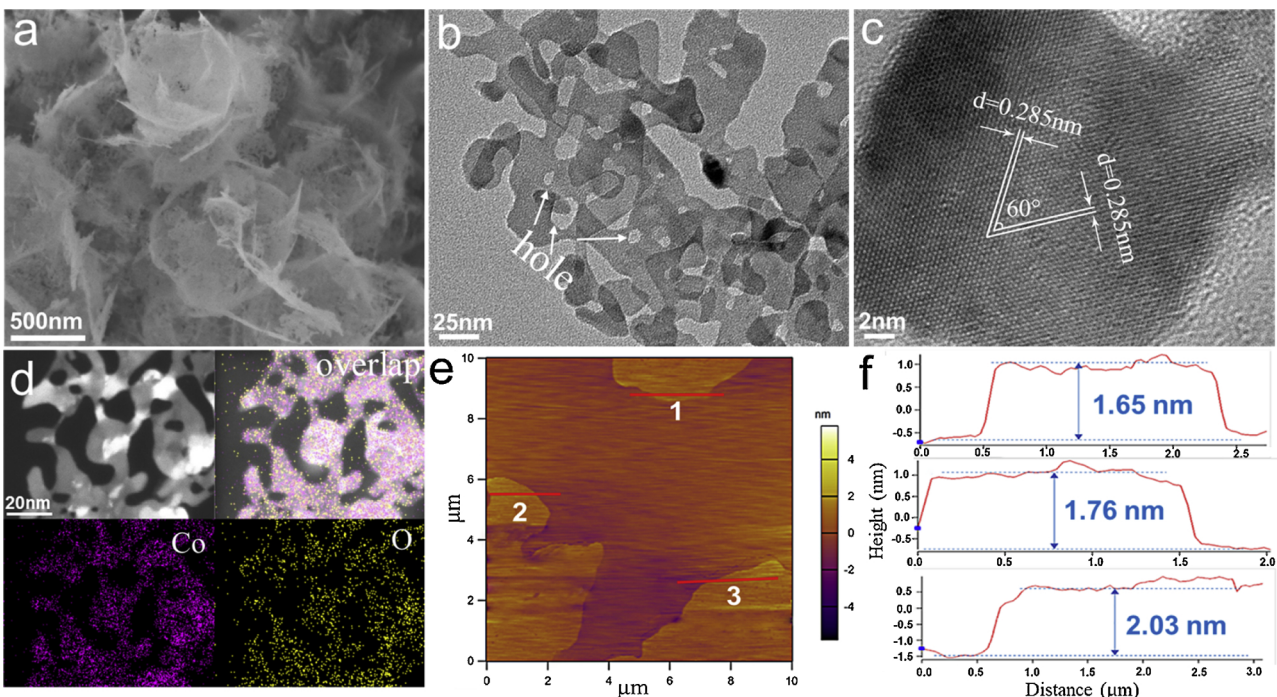


Fig. 2. (a) SEM image, (b) TEM image, (c) HRTEM image, (d) EDX mapping images (e) AFM image and (f) the corresponding height profiles of Co_3O_4 -NS (350°C); the numbers 1 to 3 in.(f) correspond to the numbers from 1 to 3 in.(e).

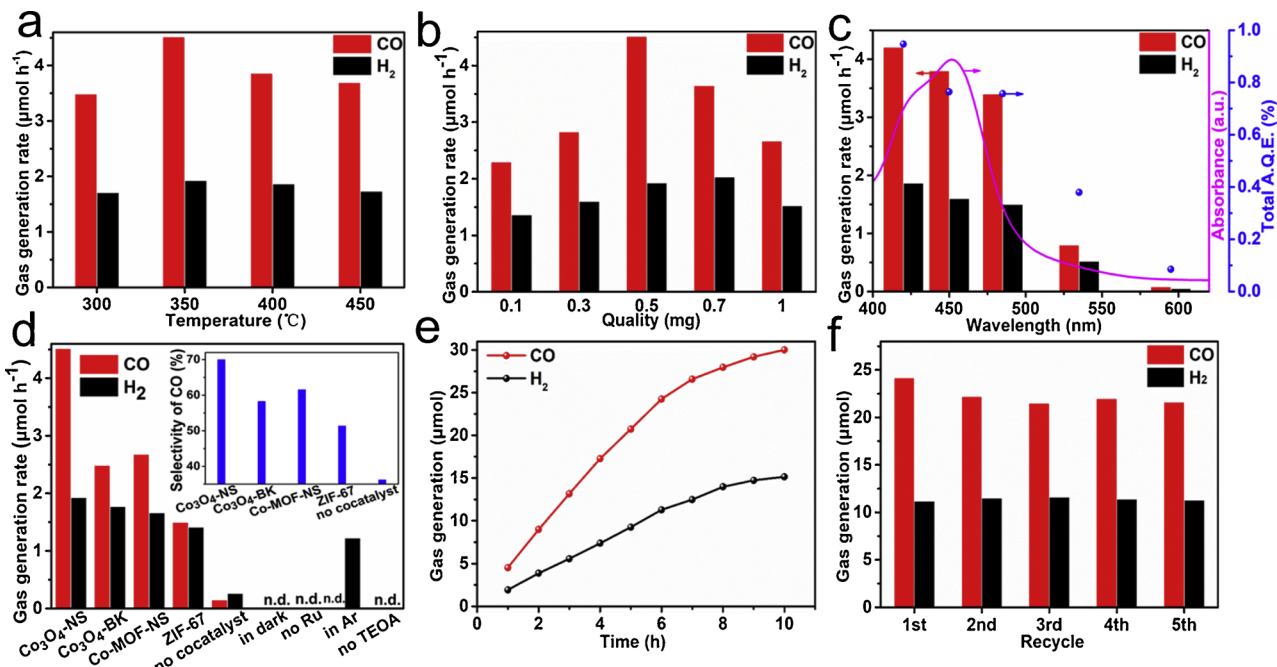


Fig. 3. (a) Influence of the Co_3O_4 -NS prepared temperature on the evolution of CO and H_2 . (b) Influence of the Co_3O_4 -NS quality on the evolution of CO and H_2 . (c) Wavelength-dependent of the CO and H_2 generation. The line is the absorption spectrum of the Ru photosensitizer. The dots are the total A.Q.E. value for each wavelength. (d) Evolution of CO and H_2 under various reaction conditions. The inset shows the CO selectivity. (e) Production of CO and H_2 as a function of reaction time. (f) Formation of CO and H_2 in stability tests (the time of each cycle is 6 h).

that the specific surface area of Co_3O_4 -NS is significantly improved compared to that of Co_3O_4 -BK. For the various Co_3O_4 -NS samples, the specific surface area drastically decreases as the calcination temperature increases, which is mainly due to the decrease in the pore volume (Table S1, SI).

The catalytic performances of the as-synthesized Co_3O_4 -NS were evaluated by visible light driven CO_2 photoreduction reactions performed in an acetonitrile/ H_2O mixture under mild reaction conditions

with TEOA and $[\text{Ru}(\text{bpy})_3]\text{Cl}_2 \cdot 6\text{H}_2\text{O}$ as the electron donor and photosensitizer, respectively. Fig. 3a shows the influence of the calcination temperature on the catalytic performance of the Co_3O_4 -NS. Apparent variations in the production rate of CO/ H_2 were observed for different samples. Comparison of the Co_3O_4 -NS samples calcined at 300 and 350°C shows that the latter exhibits better gas evolution activity because the sample annealed at 350°C has higher crystallinity (Fig. S3, SI), favouring the charge transfer in the photoredox reaction. However, the

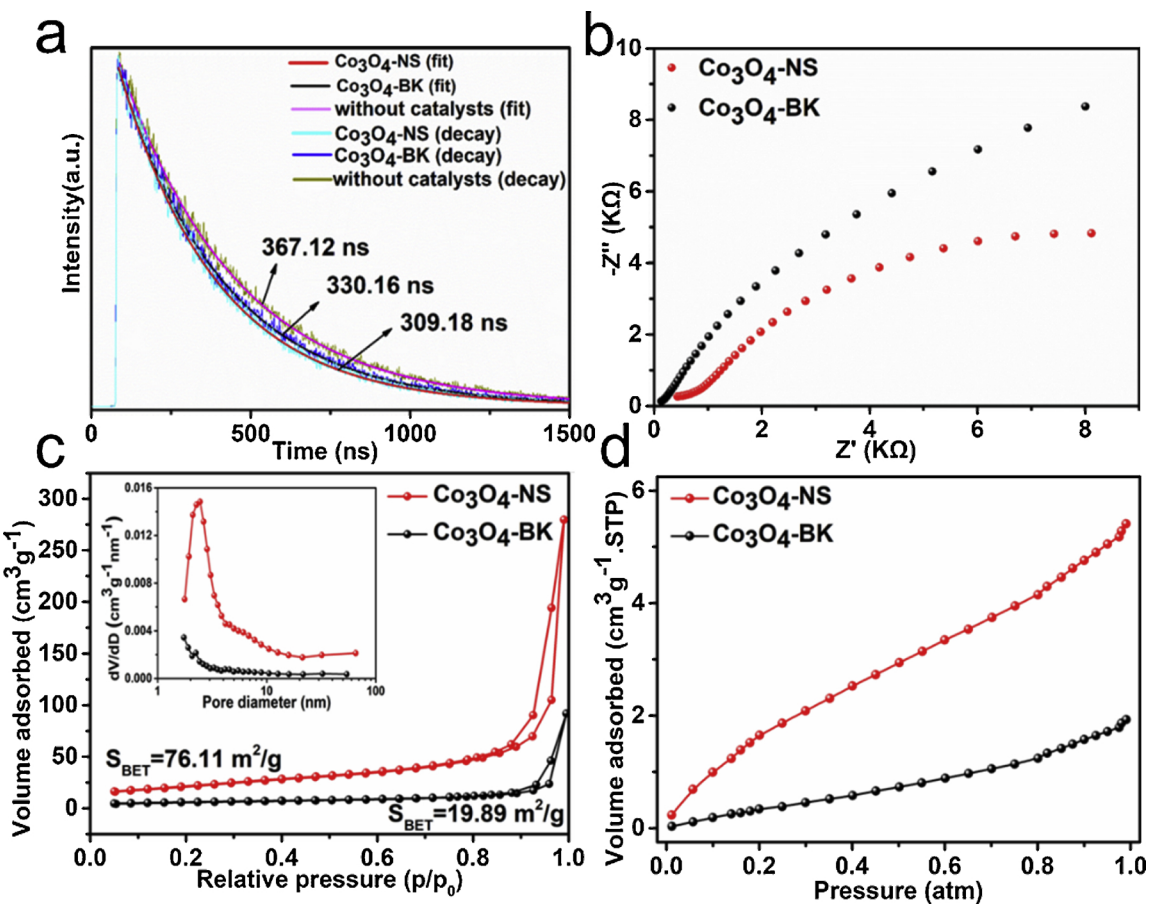


Fig. 4. (a) Time-resolved transient PL decay spectra and the corresponding fitting curves for the photocatalytic CO_2 reduction systems with $\text{Co}_3\text{O}_4\text{-NS}$, $\text{Co}_3\text{O}_4\text{-BK}$ and without catalysts under 450 nm laser irradiation. (b) Nyquist diagram of electrochemical impedance spectra for $\text{Co}_3\text{O}_4\text{-NS}$ and $\text{Co}_3\text{O}_4\text{-BK}$ modified ITO electrode in the solution containing acetonitrile/ $\text{H}_2\text{O}/\text{TEOA}$ (3:2:1, vol/vol). (c) Nitrogen adsorption-desorption isotherms and BET surface areas of $\text{Co}_3\text{O}_4\text{-NS}$ and $\text{Co}_3\text{O}_4\text{-BK}$. The inset shows the pore size distribution. (d) CO_2 adsorption isotherms of $\text{Co}_3\text{O}_4\text{-NS}$ and $\text{Co}_3\text{O}_4\text{-BK}$ at 298 K.

gas generation rate gradually decreases when the calcination temperature is further increased to 400 and 450 °C, which is closely related to the significant decrease of the specific surface area of the $\text{Co}_3\text{O}_4\text{-NS}$ caused by the higher calcination temperature (Table S1, SI). Hence, we conclude that the crystallinity and specific surface area of the $\text{Co}_3\text{O}_4\text{-NS}$ sample synergistically affect the CO_2 photoreduction performance [18]. Therefore, the optimum calcination temperature is 350 °C under the preparation conditions utilized in this study. Subsequent experiments were carried out on the samples calcined at this temperature.

The influence of the amount of the added $\text{Co}_3\text{O}_4\text{-NS}$ for the photocatalytic CO_2 reaction was also examined. As shown in Fig. 3b, even with a tiny amount (0.1 mg) of $\text{Co}_3\text{O}_4\text{-NS}$ added, the reaction system achieves the CO generation rate of $2.30 \mu\text{mol h}^{-1}$ and H_2 generation rate of $1.36 \mu\text{mol h}^{-1}$. When 0.5 mg $\text{Co}_3\text{O}_4\text{-NS}$ is included, the CO yield reached the maximum value of $4.52 \mu\text{mol h}^{-1}$ together with the H_2 generation rate of $1.93 \mu\text{mol h}^{-1}$. A further increase in the amount of $\text{Co}_3\text{O}_4\text{-NS}$ clearly decreased the amount of evolved CO. This phenomenon is mainly attributed to the fact that an insufficient amount of $\text{Co}_3\text{O}_4\text{-NS}$ lacks sufficient catalytically active sites, while excessive $\text{Co}_3\text{O}_4\text{-NS}$ can induce the light-shielding effect. Therefore, subsequent experiments were performed using 0.5 mg of added $\text{Co}_3\text{O}_4\text{-NS}$. Then, the photocatalytic properties were evaluated with five different wavelengths of the incident light. As presented in Fig. 3c, the trend in the variation of the products is fundamentally coincident with the optical absorption spectrum of the $[\text{Ru}(\text{bpy})_3]\text{Cl}_2\cdot 6\text{H}_2\text{O}$ photosensitizer, rather than that of the $\text{Co}_3\text{O}_4\text{-NS}$ sample (Fig. S7, SI). These results reveal that the photocatalytic CO_2 reduction is indeed driven by the light excitation of the dye photosensitizer, producing excited electrons to realize the

redox reactions, wherein the $\text{Co}_3\text{O}_4\text{-NS}$ acts as a mediator to facilitate the transport of electrons to reduce the absorbed CO_2 to CO [7]. Meanwhile, the maximum AQE value for CO was calculated at 420 nm (0.71%), which is higher than that of many other reported systems (Table S2, SI).

A series of control experiments were performed to further investigate the essential factors that determine the performance of the CO_2 photoreduction catalyst. When the CO_2 photoreduction reaction was carried out with $\text{Co}_3\text{O}_4\text{-NS}$ as the catalyst, the generation rate and selectivity of CO were $4.52 \mu\text{mol h}^{-1}$ and 70.1%, respectively, which are much higher than that of $\text{Co}_3\text{O}_4\text{-BK}$ ($2.48 \mu\text{mol h}^{-1}$, 58.4%) (Fig. 3d and its inset image, columns 1 and 2), indicating the importance of the Co_3O_4 structure for the reaction. Similarly, Co-MOF-NS, as a precursor of $\text{Co}_3\text{O}_4\text{-NS}$, has higher reduction performance than ZIF-67, which is a precursor of the $\text{Co}_3\text{O}_4\text{-BK}$, but both are significantly lower than $\text{Co}_3\text{O}_4\text{-NS}$ (Fig. 3d and its inset image, columns 3 and 4). Furthermore, sharp decreases in the CO generation rate ($0.14 \mu\text{mol h}^{-1}$) and CO selectivity (36.3%) were observed if the catalyst was not added to the system. These phenomena highlight the crucial role of the catalysts in the CO_2 photoreduction system (Fig. 3d and its inset image, column 5). No CO/ H_2 products are detected in the absence of visible light irradiation or photosensitizer (Fig. 3d, column 6 and 7), suggesting that the reaction is initialized by photocatalysis. When using Ar to replace CO_2 to conduct the reaction under identical conditions (Fig. 3d, column 8), only negligible amounts of H_2 are detected ($1.22 \mu\text{mol h}^{-1}$), and no detectable CO is generated. This result suggests that the generated CO originates only from the CO_2 reactant. Additionally, a control experiment was conducted without the existence of TEOA, and no generation of gas

products was detected (Fig. 3d, column 9), revealing that the sacrificial agent markedly affects the performance of the catalyst [33,45–47].

As shown in Fig. 3e, a linear relationship is observed between the CO/H₂ yield and the irradiation time over the first 6 h of the reaction. Thereafter, the CO₂-to-CO conversion rate progressively decreases, which can mainly be attributed to the exhaustion of the dye photosensitizer after a long-term reaction [7,45,47,48]. The accumulated evolution of the product is ~45 μmol after photoirradiation for 10 h. To verify this deduction, the same amount of fresh dye was added into the system after 6 h irradiation, and the reaction was continued under the same conditions. Fig. 3f shows that the CO generation retains ~90% of its original value after five runs. Simultaneously, the XRD characterization of the tested samples (Fig. S8, SI) was also conducted to gain a better understanding of the stability. No obvious differences between the tested sample and fresh sample were observed, indicating the superior stability and reusability of the Co₃O₄-NS in the photocatalytic CO₂ reduction system. Moreover, as shown in Figure S9, after photocatalytic reaction in the ¹³CO₂ (*m/z* = 45) atmosphere, mass spectrum signals of ¹³CO (*m/z* = 29) was clearly observed, indicating that the CO₂ was the source of the reduction products.

Photoelectrochemical characterizations were carried out to elucidate the origins for the higher CO₂ reduction property of Co₃O₄-NS than Co₃O₄-BK from the perspective of charge transfer kinetics. Firstly, the time-resolved PL decay spectroscopy were employed to reveal the dynamic charge behaviour in the CO₂ photoreduction systems. The emission of [Ru(bpy)₃]Cl₂·6H₂O in solution follows one exponential decay with a lifetime of 367.12 ns (Fig. 4a). However, the PL lifetime became shorter when the catalysts were added, and the Co₃O₄-NS (309.18 ns) is shorter than that of Co₃O₄-BK (330.16 ns). Also, the PL measurements were investigated to study the separation and recombination rates of the photoexcited charges. As presented in Fig. S10, the PL intensity is greatly diminished in the presence of the catalysts compared to the blank system. Furthermore, the emission intensity of the Co₃O₄-NS is lower than that of the Co₃O₄-BK. The obvious lifetime decrease and PL quenching principally indicates the remarkably suppressed electron-hole recombination [14,49,50] that augments the utilization of photoinduced electrons, thereby improving the CO₂-to-CO conversion. Conversely, the EIS spectra show that Co₃O₄-NS exhibits an obviously smaller semicircle in the Nyquist plot (Fig. 4b), indicating a

lower charge-transfer resistance in the Co₃O₄-NS system that permits fast transport and separation of interfacial charge. These results suggest that Co₃O₄-NS have a better charge transport capability which is beneficial for increasing the photocatalytic CO₂ reduction efficiency.

To further explore the factors that lead to the various performance characteristics of CO₂ photoreduction, N₂ adsorption experiments were conducted for Co₃O₄-NS and Co₃O₄-BK. As presented in Fig. 5c, over the entire relative pressure range (P/P₀), Co₃O₄-NS (279.76 cm³ g⁻¹) shows a much higher N₂ adsorption capacity than the Co₃O₄-BK (91.85 cm³ g⁻¹), mainly due to large amounts of mesopores with the pore sizes of approximately 3 nm distributed on the Co₃O₄-NS sample (inset in Fig. 4c) and the specific surface area value of the Co₃O₄-NS (76.11 cm³ g⁻¹) sample is approximately 4 times higher than that of Co₃O₄-BK (19.89 cm³ g⁻¹). The structural features of the high specific surface area and well-developed porosity allow Co₃O₄-NS to expose many more active sites for the adsorption and activation of CO₂ molecules. Therefore, to further support this hypothesis, a CO₂ adsorption experiment was performed (298 K, 1 atm). As observed from Fig. 4d, the adsorption performance of Co₃O₄-NS sample (5.41 cm³ g⁻¹) on CO₂ is approximately 3 times higher than that detected for Co₃O₄-BK (1.93 cm³ g⁻¹), which is conducive to the photochemical conversion of CO₂.

To obtain an in-depth understanding of the influence of the structural features on the photocatalytic CO₂ reduction, we performed DFT calculations to evaluate the adsorption energy (E_a) of CO₂ molecules on two Co₃O₄ crystal models: monolayer and bulk. Fig. 5 shows the optimized configurations of the CO₂ molecules adsorbed on the surface of the Co₃O₄ monolayer and Co₃O₄ bulk. Among these, the most energetically stable configurations of CO₂ absorbed on the Co₃O₄ bulk is that with one O atom coordinated with one surface Co atom (Fig. 5a), and the O-Co bond length of 2.28 Å. However, the electrons in the Co₃O₄ monolayer are more active and have a stronger ability to adsorb gas molecules [51], thus, the CO₂ molecule on the surface of the Co₃O₄ monolayer is optimized to form O-Co bond and C-O bond, with the lengths of 1.94 Å and 1.46 Å, respectively (Fig. 5b). In particular, the calculated E_a values of the Co₃O₄ bulk and Co₃O₄ monolayer were -0.13 and -0.27 eV, respectively. It is well-known that a more negative E_a value indicates a stronger CO₂ adsorption ability on the catalyst surface [52,53]. Meanwhile, we also performed DFT calculations to evaluate

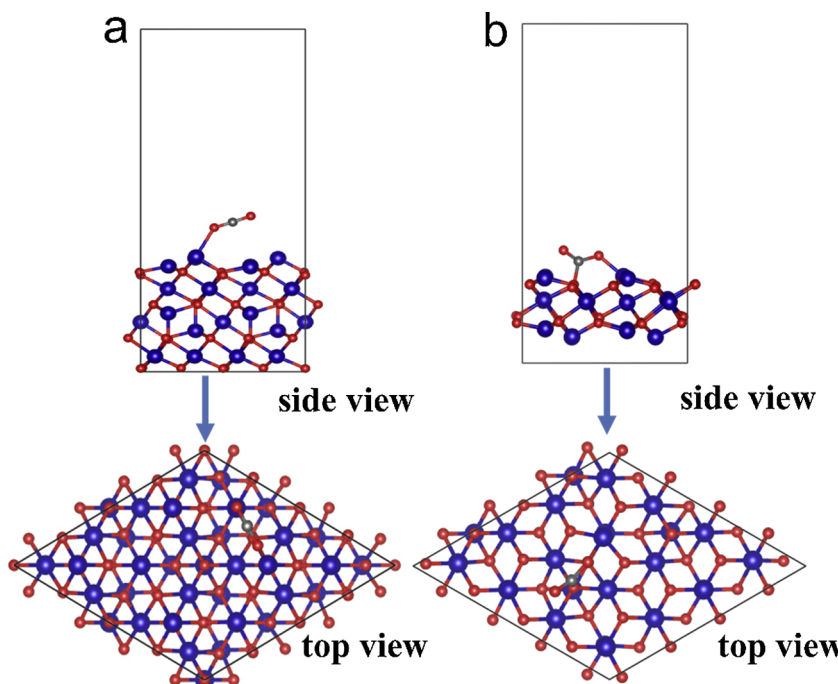


Fig. 5. Side and top views of the slab models of a single CO₂ molecule adsorbed on the surface of (a) Co₃O₄ bulk and (b) Co₃O₄ monolayer based on DFT calculations. Red, grey and blue spheres represent O, C and Co atoms, respectively. (For interpretation of the references to colour in this figure legend, the reader is referred to the web version of this article.)

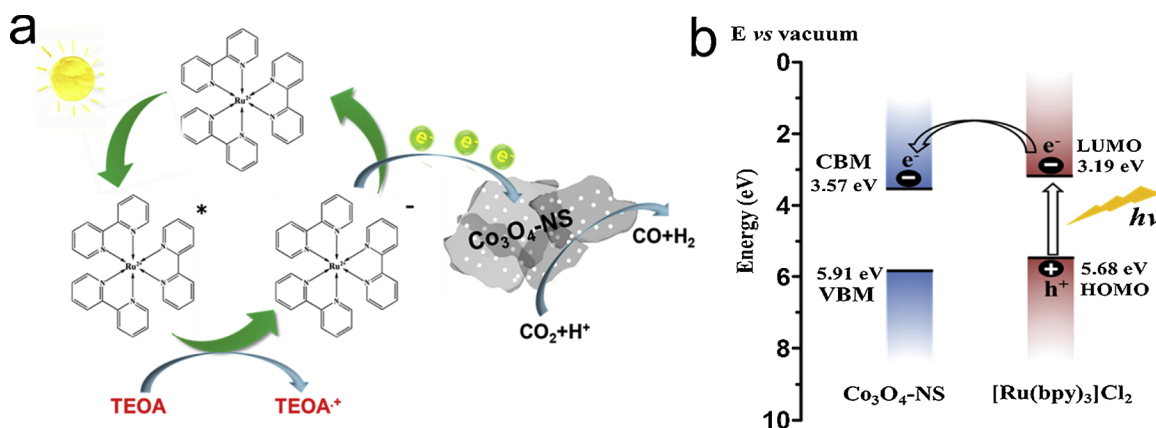


Fig. 6. (a) Proposed photocatalytic mechanism of Co₃O₄-NS with [Ru(bpy)₃]Cl₂ for the visible-light-driven photocatalytic CO₂ reduction reaction. (b) Schematic representation of energy-level diagram showing electron transfer from [Ru(bpy)₃]Cl₂ to Co₃O₄-NS. CBM: conduction band minimum; VBM: valence band maximum; LUMO: lowest unoccupied molecular orbital; HOMO: highest occupied molecular orbital.

the Ea of H atom on two Co₃O₄ crystal models (Fig.S11). The calculated values of the Co₃O₄ bulk and Co₃O₄ monolayer were -0.16 and -0.10 eV, respectively, which indicate a weaker H atom adsorption ability on Co₃O₄ monolayer (the relevant reasons were explained in the supporting information). These results suggest that Co₃O₄ monolayer is indeed more likely to adsorb CO₂ molecules under the same conditions. It should be stressed that we currently cannot rule out possible effect of crystal facets. Nevertheless, based on the fact that the more active electrons in the Co₃O₄ monolayer, we conclude that the ultrathin nanosheet structure of Co₃O₄ could bring a higher CO₂ adsorption energy during the photoreduction CO₂ reaction, which is more conducive to the photocatalytic CO₂ reduction.

Based on the above results, we propose a reasonable mechanism for the photocatalytic process (Fig. 6a). The reduction reaction starts from the excitation of the photosensitizer [Ru(bpy)₃]Cl₂ by visible-light irradiation to form the excited state that is then reductively quenched by the sacrificial electron donor TEOA to generate a reduced photosensitizer. Subsequently, the reduced photosensitizer transfers electrons to the Co₃O₄-NS, where the CO₂ molecules are adsorbed and activated. Finally, the CO₂ molecules on the surface of the Co₃O₄-NS are reduced to CO. Meanwhile, the protons in the system are also directly reduced by excited electrons to form H₂, however, the process is more difficult to proceed than the CO₂-to-CO conversion owing to a stronger affinity for CO₂ molecules by Co₃O₄-NS. Since the reduction of CO₂ is initiated by the photosensitizer, the transfer of the electrons from photosensitizer to Co₃O₄-NS is required. Therefore, the Mott-Schottky analysis was conducted to determine the flat band potential of Co₃O₄-NS. As presented in Fig. S12a, the flat band potential is calculated as ca. -0.77 V (vs. NHE), which is higher than the redox potential of E(CO₂/CO) = -0.53 V (vs. NHE) [54] and lower than that of the E(Ru(bpy)₃^{2+*/Ru(bpy)₃⁺) = -1.09 V (vs. NHE) [55]. Hence, the Co₃O₄-NS has a suitable redox potential that can accept the excited electrons from the reduced photosensitizer, thereby reducing CO₂ to CO. Furthermore, the corresponding energy level diagram (Fig. 6b) was carried out to fully explain the transfer of electrons. The conduction band minimum and the valence band maximum of Co₃O₄-NS with respect to the vacuum level were calculated to be 3.73 eV and 6.07 eV, respectively (see details in Fig. S12). Meanwhile, the lowest unoccupied molecular orbital (LUMO) and the highest occupied molecular orbital (HOMO) energy levels of [Ru(bpy)₃]Cl₂ relative to the vacuum level have been determined as 3.19 and 5.68 eV in previous studies, respectively [17,56]. Thus, the conduction band minimum of the Co₃O₄-NS is lower than the LUMO of [Ru(bpy)₃]Cl₂ so that the photoexcited electrons in the LUMO of photosensitizers could be transferred to the conduction band of Co₃O₄-NS, enabling the reduction of CO₂ subsequently. Overall, the designed Co₃O₄-NS plays two important roles in the photocatalytic}

system: 1) hosting the active sites for the photoreduction of CO₂; 2) accepting electrons from the photosensitizer and facilitating the transfer of the received electrons to CO₂ for reduction at the active sites.

4. Conclusions

We demonstrated a flexible, efficient and controllable protocol of synthesizing Co-MOF-NS-derived ultrathin Co₃O₄ nanosheets for high-efficiency photocatalytic CO₂ reduction. The prepared Co₃O₄-NS retains the distinctive structural nature of 2D structure and well-developed porosity that 1) provide a large specific surface area and high affinity to promote CO₂ adsorption, 2) shorten the diffusion length to facilitate the separation and transport of charge carriers, and 3) expose many more active sites for CO₂ photoreduction. Consequently, during the CO₂ photoreduction process, the CO₂-to-CO conversion rate of Co₃O₄-NS (4.52 μmol h⁻¹) was considerably higher than that of Co₃O₄-BK (2.48 μmol h⁻¹), and the corresponding selectivity was increased from 58.4% to 70.1%. Meanwhile, the Co₃O₄-NS exhibits a high AQE value (0.71%) and excellent stability in the reaction system. Moreover, DFT calculations reveal that the model Co₃O₄ monolayer has a stronger CO₂ adsorption energy (-0.27 eV) than the Co₃O₄ bulk (-0.13 eV), which is beneficial for the CO₂-to-CO conversion. Hence, we trust that this MOF-engaged strategy will open up new opportunities to rationally construct a large number of advanced ultrathin holey nanosheets for photocatalytic CO₂ reduction.

Acknowledgements

This work was supported by the National Natural Science Foundation of China (Grant No. 21777046 and 21836002), the Guangdong Innovative and Entrepreneurial Research Team Program (No. 2016ZT06N569), Guangzhou Science and Technology Project (No. 201803030002).

Appendix A. Supplementary data

Supplementary material related to this article can be found, in the online version, at doi:<https://doi.org/10.1016/j.apcatb.2018.12.045>.

References

- [1] W. Ong, L. Tan, Y.H. Ng, S. Yong, S. Chai, Chem. Rev. 116 (2016) 7159–7329.
- [2] R. Kuriki, M. Yamamoto, K. Higuchi, Y. Yamamoto, M. Akatsuka, D. Lu, S. Yagi, T. Yoshida, O. Ishitani, K. Maeda, Angew. Chem. Int. Ed. 56 (2017) 4867–4871.
- [3] A. Listorti, J. Durrant, J. Barber, Nat. Mater. 8 (2009) 922–929.
- [4] G. Yang, D. Chen, H. Ding, J. Feng, J.Z. Zhang, Y. Zhu, S. Hamid, D.W. Bahnemann, Appl. Catal. B: Environ. 219 (2017) 611–618.

[5] B. Han, X. Ou, Z. Deng, Y. Song, C. Tian, H. Deng, Y. Xu, Z. Lin, *Angew. Chem. Int. Ed.* 57 (2018) 16811–16815, <https://doi.org/10.1002/ange.201811545>.

[6] T. Sakakura, J. Choi, H. Yasuda, *Chem. Rev.* 107 (2007) 2365–2387.

[7] S. Wang, W. Yao, J. Lin, Z. Ding, X. Wang, *Angew. Chem. Int. Ed.* 53 (2014) 1034–1038.

[8] H. Takeda, O. Ishitani, *Coordin. Chem. Rev.* 254 (2010) 346–354.

[9] H. Takeda, K. Ohashi, A. Sekine, O. Ishitani, *J. Am. Chem. Soc.* 138 (2016) 4354–4357.

[10] V.S. Thoi, N. Kornienko, C.G. Margarit, P. Yang, C.J. Chang, *J. Am. Chem. Soc.* 135 (2013) 14413–14424.

[11] Z. Qin, C.M. Thomas, S. Lee, G.W. Coates, *Angew. Chem. Int. Ed.* 42 (2003) 5484–5487.

[12] S. Wang, B. Guan, X. Lou, *Energy Environ. Sci.* 11 (2018) 306–310.

[13] C. Gao, Q. Meng, K. Zhao, H. Yin, D. Wang, J. Guo, S. Zhao, L. Chang, M. He, Q. Li, H. Zhao, X. Huang, Y. Gao, Z. Tang, *Adv. Mater.* 28 (2016) 6485.

[14] C. Gao, S. Chen, Y. Wang, J. Wang, X. Zheng, J. Zhu, L. Song, W. Zhang, Y. Xiong, *Adv. Mater.* 30 (2018) 4624.

[15] S. Wang, X. Wang, *Angew. Chem. Int. Ed.* 55 (2016) 2308–2320.

[16] J. Qin, S. Wang, X. Wang, *Appl. Catal. B: Environ.* 209 (2017) 476–482.

[17] K. Zhao, S. Zhao, C. Gao, J. Qi, H. Yin, D. Wei, M.F. Mideksa, X. Wang, Y. Gao, Z. Tang, R. Yu, *Small* (2018) 1800762.

[18] S. Wang, Y. Hou, X. Wang, *ACS Appl. Mater. Interface* 7 (2015) 4327–4335.

[19] S. Wang, Z. Ding, X. Wang, *Chem. Commun.* 51 (2015) 1517–1519.

[20] B. Han, S. Liu, N. Zhang, Y. Xu, Z. Tang, *Appl. Catal. B: Environ.* 202 (2017) 298–304.

[21] H. Zhang, *ACS Nano* 9 (2015) 9451–9469.

[22] Z. Sun, N. Talreja, H. Tao, J. Texter, M. Muhler, J. Strunk, J. Chen, *Angew. Chem. Int. Ed.* 57 (2018) 7610–7627.

[23] Y. Chen, G. Jia, Y. Hu, G. Fan, Y. Tsang, Z. Li, Z. Zhou, *Sustain. Energy Fuels* 1 (2017) 1875.

[24] Y. Zhou, Y. Zhang, M. Lin, J. Long, Z. Zhang, H. Lin, J.C. Wu, X. Wang, *Nat. Commun.* 6 (2015) 7873.

[25] S. Liang, L. Wen, S. Lin, J. Bi, P. Feng, X. Fu, L. Wu, *Angew. Chem. Int. Ed.* 53 (2014) 2951–2955.

[26] J. Zhang, Y. Chen, X. Wang, *Energy Environ. Sci.* 8 (2015) 3092–3108.

[27] S. Qamar, F. Lei, L. Liang, S. Gao, K. Liu, Y. Sun, W. Ni, Y. Xie, *Nano Energy* 26 (2016) 692–698.

[28] Q. Liang, Z. Li, Z. Huang, F. Kang, Q. Yang, *Adv. Funct. Mater.* 25 (2015) 6885–6892.

[29] G. Zhan, H.C. Zeng, *Adv. Funct. Mater.* 26 (2016) 3268–3281.

[30] G. Yilmaz, K. Yam, C. Zhang, H. Fan, G. Ho, *Adv. Mater.* 29 (2017) 1606814.

[31] G. Anandhababu, Y. Huang, D.D. Babu, M. Wu, Y. Wang, *Adv. Funct. Mater.* 28 (2018) 1706320.

[32] Y. Su, D. Ao, H. Liu, Y. Wang, *J. Mater. Chem. A* 5 (2017) 8680–8689.

[33] S. Xiao, D. Pan, R. Liang, W. Dai, Q. Zhang, G. Zhang, C. Su, H. Li, W. Chen, *Appl. Catal. B: Environ.* 236 (2018) 304–313.

[34] Z. Xie, W. Xu, X. Cui, Y. Wang, *Chemsuschem.* 10 (2017) 1645–1663.

[35] K. Tao, X. Han, Q. Cheng, Y. Yang, Z. Yang, Q. Ma, L. Han, *Chem. Eur. J.* 24 (2018) 12584–12591, <https://doi.org/10.1002/chem.201800960>.

[36] C. Tan, H. Zhang, *Nat. Commun.* 6 (2015) 8340.

[37] F. Cao, M. Zhao, Y. Yu, B. Chen, Y. Huang, J. Yang, X. Cao, Q. Lu, X. Zhang, Z. Zhang, C. Tan, H. Zhang, *J. Am. Chem. Soc.* 138 (2016) 6924–6927.

[38] J. Yang, F. Zhang, H. Lu, X. Hong, H. Jiang, Y. Wu, Y. Li, *Angew. Chem. Int. Ed.* 54 (2015) 10889–10893.

[39] X. Xiao, C. He, S. Zhao, J. Li, W. Lin, Z. Yuan, Q. Zhang, S. Wang, L. Dai, D. Yu, *Energy Environ. Sci.* 10 (2017) 893–899.

[40] Y. Dou, T. Liao, Z. Ma, D. Tian, Q. Liu, F. Xiao, Z. Sun, J.H. Kim, S.X. Dou, *Nano Energy* 30 (2016) 267–275.

[41] S. Wendt, P.T. Sprunger, E. Lira, G.K.H. Madsen, Z. Li, J.O. Hansen, J. Matthiesen, A. Blekinge-Rasmussen, E. Laegsgaard, B. Hammer, F. Besenbacher, *Science* 320 (2008) 1755–1759.

[42] W. Wei, W. Chen, D.G. Ivey, *Chem. Mater.* 20 (2008) 1941–1947.

[43] S. Gao, X. Jiao, Z. Sun, W. Zhang, Y. Sun, C. Wang, Q. Hu, X. Zu, F. Yang, S. Yang, L. Liang, J. Wu, Y. Xie, *Angew. Chem. Int. Ed.* 55 (2016) 698–702.

[44] J. Xu, P. Gao, T. Zhao, *Energy Environ. Sci.* 5 (2012) 5333–5339.

[45] T. Ouyang, H. Huang, J. Wang, D. Zhong, T. Lu, *Angew. Chem. Int. Ed.* 56 (2017) 738–743.

[46] H. Xu, J. Hu, D. Wang, Z. Li, Q. Zhang, Y. Luo, S. Yu, H. Jiang, *J. Am. Chem. Soc.* 137 (2015) 13440–13443.

[47] Y. Wang, N. Huang, J. Shen, P. Liao, X. Chen, J. Zhang, *J. Am. Chem. Soc.* 140 (2018) 38–41.

[48] X. Lin, Y. Gao, M. Jiang, Y. Zhang, Y. Hou, W. Dai, S. Wang, Z. Ding, *Appl. Catal. B: Environ.* 224 (2018) 1009–1016.

[49] J. Hou, S. Cao, Y. Wu, F. Liang, L. Ye, Z. Lin, L. Sun, *Nano Energy* 30 (2016) 59–68.

[50] L. Ye, Y. Gao, S. Cao, H. Chen, Y. Yao, J. Hou, L. Sun, *Appl. Catal. B: Environ.* 227 (2018) 54–60.

[51] S. Gao, X. Jiao, Z. Sun, W. Zhang, Y. Sun, C. Wang, Q. Hu, X. Zu, F. Yang, S. Yang, L. Liang, J. Wu, Y. Xie, *Angew. Chem. Int. Ed.* 55 (2016) 698–702.

[52] P. Xia, B. Zhu, J. Yu, S. Cao, M. Jaroniec, *J. Mater. Chem. A* 5 (2017) 3230–3238.

[53] H. Wu, L. Liu, S. Zhao, *Phys. Chem. Chem. Phys.* 16 (2014) 3299–3304.

[54] J. Schneider, H. Jia, J.T. Muckerman, E. Fujita, *Chem. Soc. Rev.* 41 (2012) 2036–2051.

[55] C. Creutz, N. Sutin, *Inorg. Chem.* 15 (1976) 496–499.

[56] D.A. Bernards, S. Flores-Torres, H.D. Abruna, G.G. Malliaras, *Science* 313 (2006) 1416–1419.